PHYSICAL REVIEW APPLIED **11,** 034013 (2019)

Proposal for the Realization of a Single-Detector Acoustic Camera Using a Space-Coiling Anisotropic Metamaterial

Tianxi Jiang,[1] Qingbo He,[2,*] and Zhi-Ke Peng[2]

[1] *Department of Precision Machinery and Precision Instrumentation, University of Science and Technology of China, Hefei 230026, People's Republic of China*

[2] *State Key Laboratory of Mechanical System and Vibration, Shanghai Jiao Tong University, Shanghai 200240, People's Republic of China*

(Received 11 July 2018; revised manuscript received 10 December 2018; published 6 March 2019)

Acoustic imaging is crucial in diverse applications, such as target tracking, clinical treatment, and structural health monitoring. Current approaches mainly use complex and large transducer arrays. A space-coiling anisotropic metamaterial with stochastic structural parameters is proposed to realize a single-detector acoustic camera. Analytical and numerical results demonstrate that the high anisotropy based on the space-coiling method enables the metamaterial to produce an orthogonal directional modulation for input acoustic waves. Thus, the information of sound sources can be reconstructed from the modulated mixed signals by means of a compressive sensing framework. Experimental results show that the localization and imaging of multiple broadband sources can be achieved in azimuthal and planar geometries. The metamaterial-based single-detector acoustic camera expands the capabilities of single-detector acoustic imaging, thereby opening avenues for designing an alternative class of acoustic sensing systems.

DOI: 10.1103/PhysRevApplied.11.034013

I. INTRODUCTION

Acoustic imaging is critically needed in diverse applications, including acoustic target tracking [1], clinical treatment [2], and structural health monitoring [3]. Current approaches for realizing acoustic imaging are mainly based on an acoustic camera, a device that generally consists of a transducer array with imaging algorithms [3–7]. The use of multiple transducers imposes strict requirements for simultaneous data acquisition. The spatial resolution of acoustic imaging depends on the number of transducers and the array dimensions. The complexity and very large dimensions of the system are major disadvantages that limit the applications of acoustic cameras. Efforts have been made to overcome the shortcomings of the transducer array by developing devices with unusual properties. Bionic microphones were utilized for azimuthal estimation based on the hearing systems of the parasitic fly *Ormia ochracea* and the gecko [8–10]. The size of a bionic microphone can be considerably smaller than the wavelength of the incident sound wave, but still provide sufficient cues for sound localization due to the mechanically coupled vibration of the structure. In addition to bionic microphones, studies have achieved directional acoustic sensing by placing a single detector in an artificial anisotropic acoustic structure [11–13]. However, the working bandwidths of these devices are limited to structural resonance frequencies. The requirement of active scanning and the incapability to separate overlapping signals from multiple sources are two other problems.

Recently, a technique, namely, single-pixel compressive imaging, has been developed by using one detector instead of multiple detectors for electromagnetic computational imaging [14–16]. One-dimensional (1D), two-dimensional (2D), and three-dimensional (3D) acoustic imaging have been successfully demonstrated by utilizing the imaging algorithms coupled to spatially encoded scattering masks [17–19]. However, the size of the scatterers typically needs to be larger than the wavelengths involved [18,19]; otherwise, diffraction effects must be considered [17]. The device will be large when working at low frequencies. This problem can be solved by using acoustic metamaterials. Acoustic metamaterials are artificial structures that comprise subwavelength blocks with homogenized unusual properties and functionalities that are not found in nature [20–26]. Fascinating applications, such as cloaking [27–29], beam steering [30], diffusing [31], and logical control [32–34], have been proposed and demonstrated. For single-detector acoustic imaging, acoustic metamaterials can achieve the spatial encoding of acoustic waves on a subwavelength scale compared with scattering masks. A broadband metamaterial-based single-detector device was proposed by producing an orthogonal directional acoustic modulation with multiple arrays of Helmholtz resonators [35]. The device can solve the azimuthal multispeaker

---

[*] qbhe@sjtu.edu.cn

listening problem by combining a compressive sensing framework, which opens up an alternative approach to broadband single-detector acoustic imaging. However, the frequency modulation is determined by the lengths of the Helmholtz resonators. The height of the device depends on the longest resonator, which is not suitable to be extended to planar acoustic imaging. Single-detector acoustic imaging in azimuthal and planar geometries with metamaterial-based devices remains unexplored.

Here, we demonstrate a space-coiling anisotropic metamaterial to realize a single-detector acoustic camera for azimuthal and planar acoustic imaging. The metamaterial is designed by assembling different fan-shaped space-coiling acoustic channel modules comprised of unit cells with stochastic structural parameters (Fig. 1). We use the term "metamaterial" to describe the proposed system, because the aperture size A and total length of the fan-shaped module L for the maximum wavelength involved are $\lambda/7.5$ and $\lambda/1.7$, respectively [36,37]. The structural randomness of the space-coiling metamaterial makes its effective acoustic parameters highly anisotropic, thereby enabling orthogonal directional modulation of the incident sound waves. The information of the sound sources can be reconstructed from the modulated mixed signals by using a compressive sensing framework. We experimentally demonstrate that the metamaterial-based single-detector system is capable of imaging similar to an acoustic camera for multiple broadband sound sources. This study broadens the scope of single-detector acoustic imaging and can be applied to numerous acoustic engineering fields.

II. RESULTS

A. Design of the space-coiling anisotropic metamaterial

Figure 1(a) shows that the proposed metamaterial is comprised of 36 fan-shaped modules with space-coiling acoustic channels. Each acoustic channel module includes 10 different unit cells as shown in Fig. 1(b). The unit cells are numbered $1\sim n$ from the inside to the outside of each module. The inner radius of the nth unit cell is represented as $R_n = R_1 + (n-1)\,\Delta R$, where $R_1 = 35$ mm is the inner radius of the fan-shaped module, and $\Delta R = 10$ mm is the overall length of the unit cell. Thus, the radius of the entire metamaterial is 135 mm. The height of the metamaterial is designed to be 12 mm, corresponding to $\lambda/14.3$ for 2000 Hz. The turning angle of the folded channel is β_n, which is a stochastic variable dominating the length L_n of the acoustic-wave trajectory highlighted by the red solid line in Fig. 1(b). Based on the effective medium theory, the nth unit cell can be equivalent to a homogeneous medium with an effective refractive index n_{eff}^n and an effective mass density ρ_{eff}^n. It has been demonstrated that the effective parameters can be calculated using the path length of the acoustic wave [25,38]. n_{eff}^n and ρ_{eff}^n of the nth unit cell

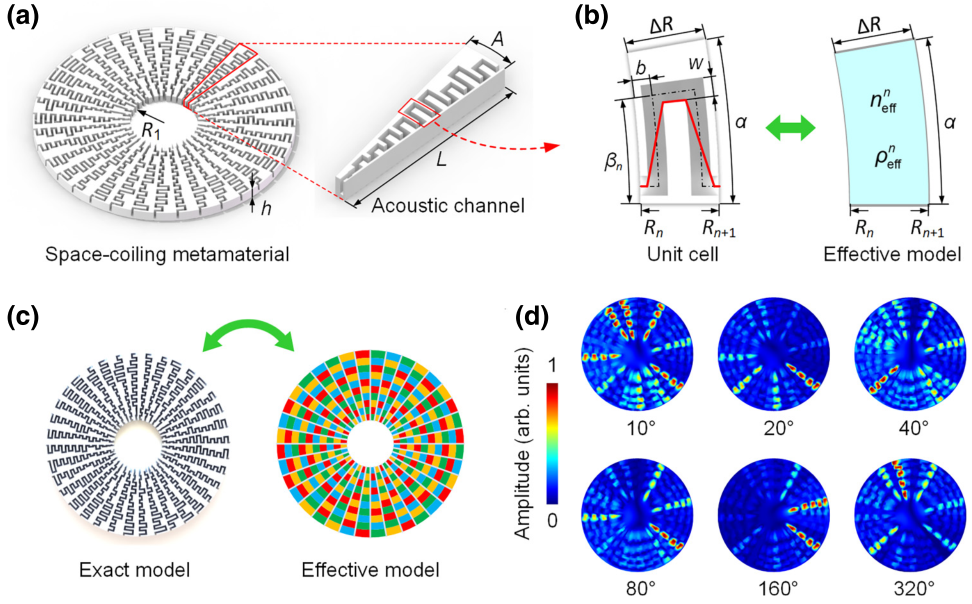

FIG. 1. Space-coiling anisotropic metamaterial. (a) Schematic diagram of the space-coiling metamaterial. The metamaterial is comprised of 36 fan-shaped modules with space-coiling acoustic channels. The aperture size A of the fan-shaped module is 23.6 mm. The total length of the fan-shaped module L is 100 mm. The inner radius of the acoustic channel is $R_1 = 35$ mm and the height of the metamaterial is $h = 12$ mm. (b) The unit cell and the effective model. The dimensions of the unit cell are determined as $\Delta R = 10$ mm, $w = 2.5$ mm, $b = 2.25$ mm, and $\alpha = 10°$. (c) The effective model of the metamaterial. (d) Acoustic modes under different incident angles at 3725 Hz.

can be expressed as:

$$n_{\text{eff}}^{n} = L_n/\Delta R, \tag{1}$$

$$\rho_{\text{eff}}^{n} = \frac{\pi(R_n + R_{n+1})}{Mw} n_{\text{eff}}^{n} \rho_0 \,, \tag{2}$$

where L_n is a function of the stochastic variable β_n; M is the channel number of the metamaterial; w is the channel width; ρ_0 is the density of air. The transfer matrix method (TMM) is used to derive the analytical transmission coefficient of the module comprised of 10 unit cells [37]. In this method, the transfer matrix of the nth unit cell is obtained and the transfer matrix of the entire acoustic channel module is consequently derived (see Appendix A for the analytical derivation). By applying boundary conditions, the transmission coefficient of one module is given by:

$$T = \frac{2}{M_{11} + M_{12}/\rho_0 c_0 + \rho_0 c_0 M_{21} + M_{22}}, \tag{3}$$

where c_0 is the sound speed of air; M_{ij} are elements of the transfer matrix of the module. The amplitude of the transmission coefficient is denoted as $T_{\text{amp}} = |T|$. The transmissions obtained by the TMM and the numerical calculation of the exact model have a high degree of agreement (Appendix A). The results demonstrate that the transmissions of different modules are orthogonal. The structural randomness of the unit cell essentially leads to stochastic effective acoustic parameters. The entire metamaterial is highly anisotropic by assembling different modules. As a result, the frequency responses of the metamaterial can be sensitive to direction.

Direction-sensitive frequency responses of the entire metamaterial are obtained through numerical calculations (see Fig. S1 of the Supplemental Material [39]). The average cross-correlation coefficient of the direction-sensitive frequency responses is approximately 0.20 for the metamaterial, indicating that the modulation effect of the sound waves is orthogonal under different incidences. Figure 1(c) shows an effective model of the metamaterial. The simulated frequency responses of the effective model are consistent with the exact model (Appendix A), indicating that the effective model can accurately reflect the anisotropic acoustic property of the space-coiling metamaterial. Figure 1(d) presents the simulated acoustic modes of the exact model under different incidences at 3725 Hz. Substantial differences exist among the acoustic modes even if the incident angles differ by 10°. This property guarantees a sufficient resolution for acoustic imaging. The orthogonal directional acoustic modulation is due to the high anisotropy of the space-coiling metamaterial, which results in the realization of a desirable single-detector acoustic compressive imaging.

B. Metamaterial-based single-detector acoustic compressive imaging

The general procedure of the metamaterial-based single-detector acoustic compressive imaging is illustrated in Fig. 2. A single detector is placed inside the center of the anisotropic metamaterial. The input sound waves emitted from multiple sound sources are directionally modulated by the metamaterial in amplitude and then collected by the central detector. The metamaterial-based sensing system is appropriate for the framework of compressive sensing due to the sparsity of sound sources and the orthogonality of the modulation effect. We describe the sensing system as

$$\mathbf{y} = \mathbf{M}\mathbf{x}, \tag{4}$$

where $\mathbf{y}$ is the observation vector; $\mathbf{M}$ is the measurement matrix determined by the metamaterial and the testing signals; $\mathbf{x}$ is the object vector to be estimated. An audio library

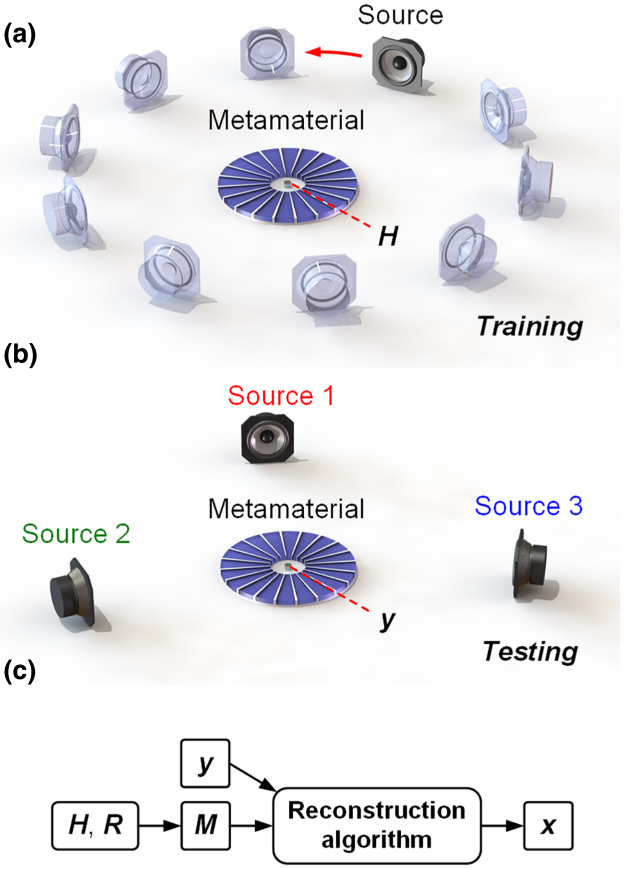

FIG. 2. Procedure schematic diagram of the metamaterial-based single-detector acoustic compressive imaging. (a) The training process to obtain the directional frequency response $\mathbf{H}$ of the metamaterial for constructing the measurement matrix. (b) The testing process to estimate the performance of the sensing system. (c) Schematic of the entire procedure. The object vector $\mathbf{x}$ is estimated by the reconstruction algorithm.

is established to store the testing sound signals, the spectra of which form a matrix **R**. For single-detector acoustic compressive imaging, it is important to know the *a priori* measurement matrix. Here, the measurement matrix **M** is constructed by the directional frequency response **H** of the metamaterial and the testing signal matrix **R** (Appendix B). The directional frequency response **H** is obtained by playing the source in different locations as shown in Fig. 2(a), whereas the matrix **R** is measured by playing the testing signals in free space. This process can be described as training. After training, a sequence of sounds in the audio library is simultaneously generated from the sources to examine the performance of the sensing system, as shown in Fig. 2(b). This process is described as testing, where the observation vector **y** is obtained. The compressive sensing concept can be introduced to solve Eq. (4) for estimating the object vector **x** because sound sources are sparse and the correlation between each column of the measurement matrix is small enough. Estimation is performed to reconstruct the audio content of each source from the mixed signal by using the inverse signal processing algorithm. The solution to Eq. (4) can be obtained with an L1-norm minimization:

$$\hat{\mathbf{x}} = \min||\mathbf{x}||_1 \quad \text{s.t. } \mathbf{Mx} = \mathbf{y}\,, \tag{5}$$

where $\hat{\mathbf{x}}$ is the solution of the unknown $\mathbf{x}$, and $||\mathbf{x}||_1$ denotes the L1-norm $\sum_i|\mathbf{Mx}_i - \mathbf{y}_i|$ of $\mathbf{x}$. Many methods exist to solve the inverse problem of Eq. (5) based on the compressive sensing theory. The nonzero elements in **x** contain the information of potential locations and signal labels of sources. The entire procedure of the metamaterial-based single-detector acoustic compressive imaging is summarized in Fig. 2(c).

An experiment is conducted in an anechoic chamber to verify the acoustic imaging performance of the metamaterial-based single-detector sensing system according to the preceding procedure as shown in Fig. 3(a). The metamaterial is fabricated with poly-lactic acid (PLA) plastics by using fused-filament-fabrication 3D printing. Broadband input sound waves generated from a speaker are coupled into the metamaterial from free space. Two microelectromechanical microphones (Analog Devices, ADMP401) are placed inside and outside the metamaterial with their *z* axis perpendicular to the ground to pick up the observed signal and the referenced signal, respectively. Because of the unavoidable visco-thermal effects [40] and the manufacturing tolerance, the actual frequency responses of the metamaterial are different from the numerical simulations. The training process should be experimentally performed in advance to obtain the actual measurement matrix. The directional frequency responses of the metamaterial are shown in Fig. 3(b), where the average cross-correlation coefficient is approximately 0.33. In the testing process, a bird tweet and a machine vibration signal are successively emitted at 36 different locations (every two locations differ by 10°) to test the performance of the metamaterial-based sensing system. Waveforms and frequency spectra of the two signals are provided in Fig. S2 of the Supplemental Material [39]. The two-step iterative shrinkage/thresholding (TWIST) algorithm is used to reconstruct the audio message of each source, which includes the information of the source location [41]. The reconstruction results of the bird tweet and the machine

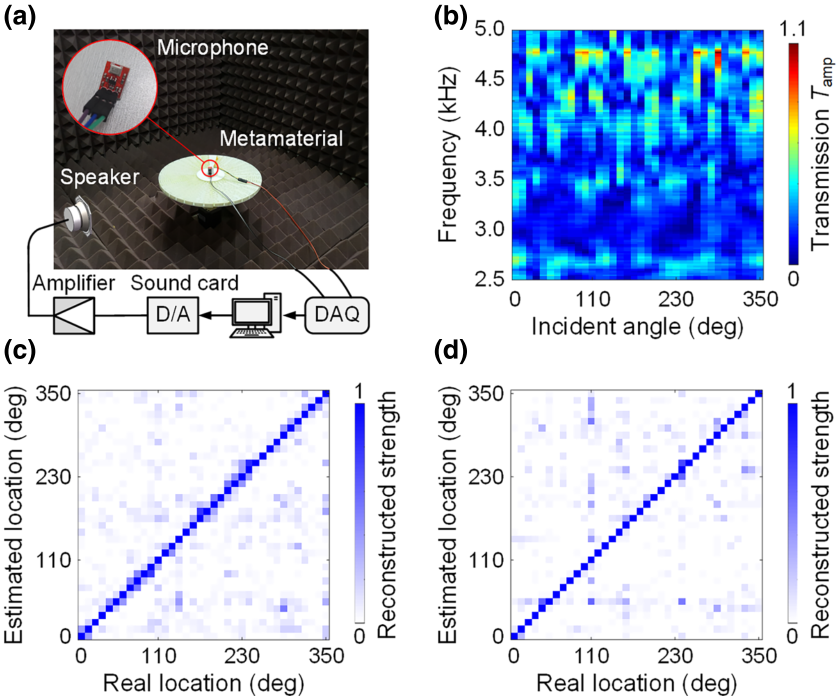

FIG. 3. Experimental results of single-source recognition. (a) The schematic diagram of the experimental setup. (b) The measured directional frequency response of the metamaterial. Reconstruction results for (c) the bird tweet and (d) the machine vibration signals, respectively.

vibration signals are shown in Figs. 3(c) and 3(d). The estimated location, where the reconstruction strength is the strongest, agrees well with the real location of the sources. More details about the reconstruction results can be found in the Supplemental Material [39]. The results preliminarily verify that the metamaterial-based single-detector sensing system can recognize azimuths of broadband sound sources, which lays the foundation for multiple source recognition and imaging.

C. Recognition of azimuthal multiple sound sources

Recognition tasks of azimuthal multiple sound sources are experimentally conducted to examine the performance of the space-coiling metamaterial-based single-detector sensing system. Twenty-four different bird tweets with normalized energy are collected in an audio library as testing signals (waveforms and spectra are provided in Fig. S4 of the Supplemental Material [39]). Figure 4(a) shows the task to identify the locations of three sources and segregate the overlapping signals at the same time. The testing signals are randomly selected from the audio library and simultaneously emitted by three speakers. The mixed signal measured by the central microphone contains the messages of the locations and audio contents of the three sources. The reconstruction algorithm recovers the audio messages and the results are shown in Fig. 4(a) (see Supplemental Material [39] for more details). A darker color means a higher signal strength. The recognized audio is defined as the audio whose highest reconstructed strength matches the truth for each source in every experiment. The recognition ratio can thus be calculated as the number of the recognized audios over the total number of the audio messages. For this task, the recognition ratio is 96.7%. Figure 4(b) shows the task to reconstruct the audio messages of two or three randomly selected sources out of four possible locations. Here, a successful recognition is defined as one for which the highest reconstructed strength

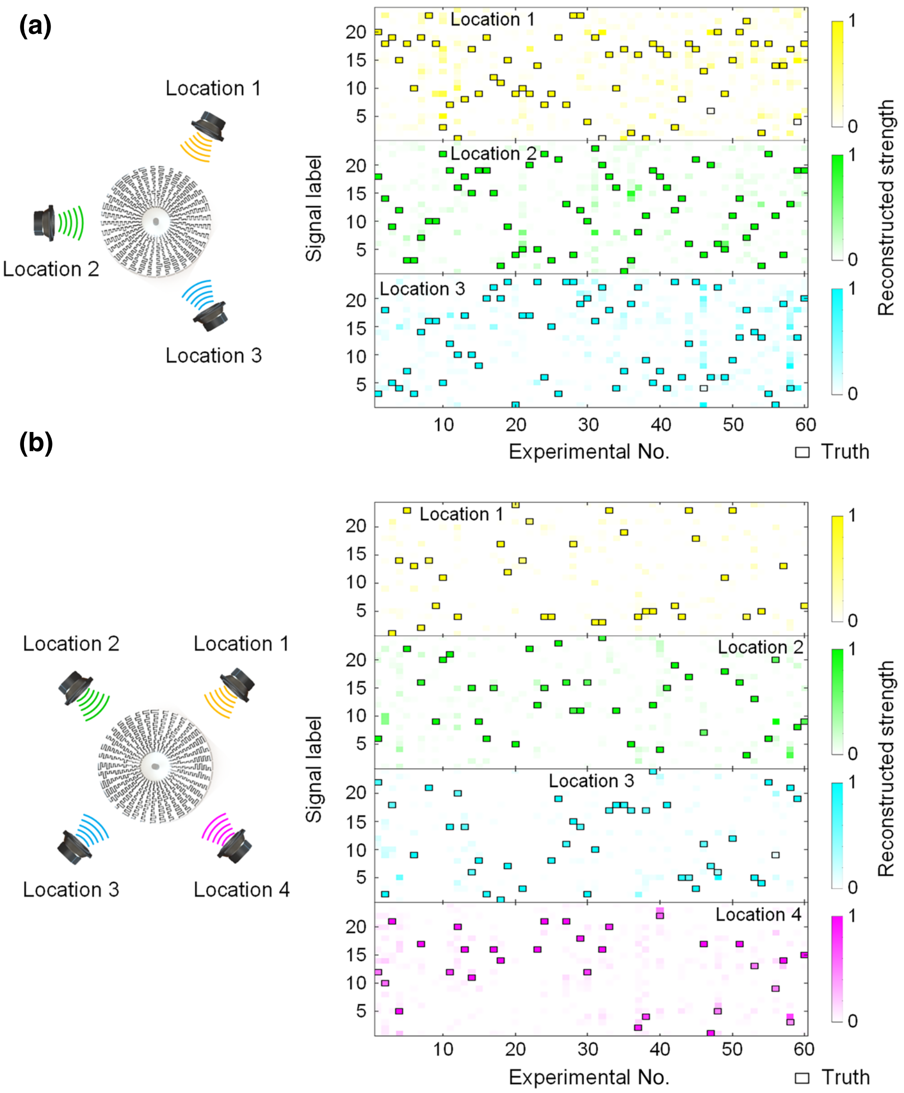

FIG. 4. Recognition performance for azimuthal multiple sources. (a) The recognition task of three sources and the reconstruction results. (b) The recognition task to reconstruct the audio messages of two or three randomly selected sources out of four possible locations.

of the activated source is above 0.5 (whereas it is below 0.2 for the silence source) and matches the truth. The recognition ratio calculated using the above definition is 95.8%. In addition, more recognition tasks and results can be found in Fig. S6 of the Supplemental Material [39]. The above results demonstrate that the metamaterial-based single-detector sensing system is capable of identifying locations and simultaneously separating audio contents from the mixed signal, which is desirable to solve multispeaker listening problems (e.g., the "cocktail party" problem).

D. Planar acoustic imaging

The proposed metamaterial prototype has a deep-subwavelength scale in height (corresponding to λ/14.3 for 2000 Hz and λ/5.7 for 5000 Hz). Thus, the single-detector acoustic camera can be realized by stacking different metamaterial samples for planar acoustic imaging as shown in Fig. 5(a). A single microphone is placed in the cavity behind the stacked metamaterial structure. The metamaterial-based single-detector acoustic camera modulates the sound waves in two dimensions (i.e., azimuthal and pitching angles), which can be used for planar acoustic imaging. Figure 5(b) shows the schematic of the planar acoustic imaging experiment. The objective plane is 0.8 m away from the stacked metamaterial-based single-detector acoustic camera and is meshed as 5 × 5 grids as shown in Fig. 5(c), hence the angular resolution is about 11.4°. The sound source can be positioned at the center of the grid, generating specific broadband white noises as testing signals. The training process is conducted by traversing all grids with the source to construct the measurement matrix. After that, the testing process is performed by randomly positioning one or two sources in the grids. The single source imaging results are shown in Fig. 5(d). The darkest color block indicates the most probable location of the source. The estimated results are in agreement with the actual source locations. Figure 5(e) shows the imaging results of two sources emitting sounds simultaneously. The reconstructed strength of the estimated object vector $\mathbf{x}$ should be analyzed to distinguish which source is located at what position (Appendix C). When two sources are relatively far apart from each other (e.g., the sources are in the 16th and 10th grids), we can determine the locations of the sources by comparing the substantial energy differences in the reconstructed strength. When two sources are too close to each other (e.g., the sources are in the 17th and 12th grids), the reconstructed strength difference is so small that the source of the signal cannot be distinguished. Nonetheless, the imaging results in Fig. 5(e) clearly show the existence of two sources.

The imaging performance of the metamaterial-based single-detector acoustic camera is also investigated by using sound sources with different amplitudes as well as different positions. Here, three tasks are performed as shown in Fig. 6. The objective plane with an area of 0.8×0.8 m^2 is meshed as 6×6 grids with an angular resolution of 9.5°. The first task is schematically illustrated in Fig. 6(a). A testing signal is sequentially emitted

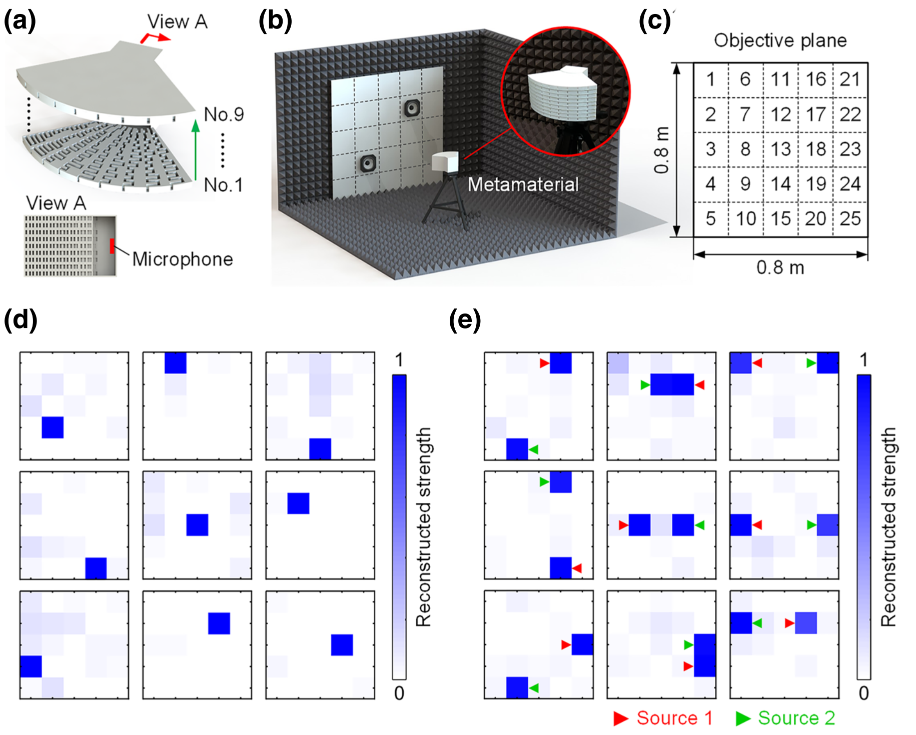

1	6	11	16	21
2	7	12	17	22
3	8	13	18	23
4	9	14	19	24
5	10	15	20	25

FIG. 5. Planar acoustic imaging of the metamaterial-based single-detector acoustic camera. (a) The metamaterial-based single-detector acoustic camera for planar acoustic imaging is fabricated by stacking nine metamaterial samples to produce 2D modulations of the acoustic waves. View A shows the section of the stacked metamaterial structure where a single microphone is positioned in the cavity behind the metamaterial structure. (b) The schematic experimental setup of the planar acoustic imaging. (c) The meshing and numbering of the objective plane. (d) The recognition results of the single source. (e) The recognition results of two sources. The actual locations of the sources are marked by triangles.

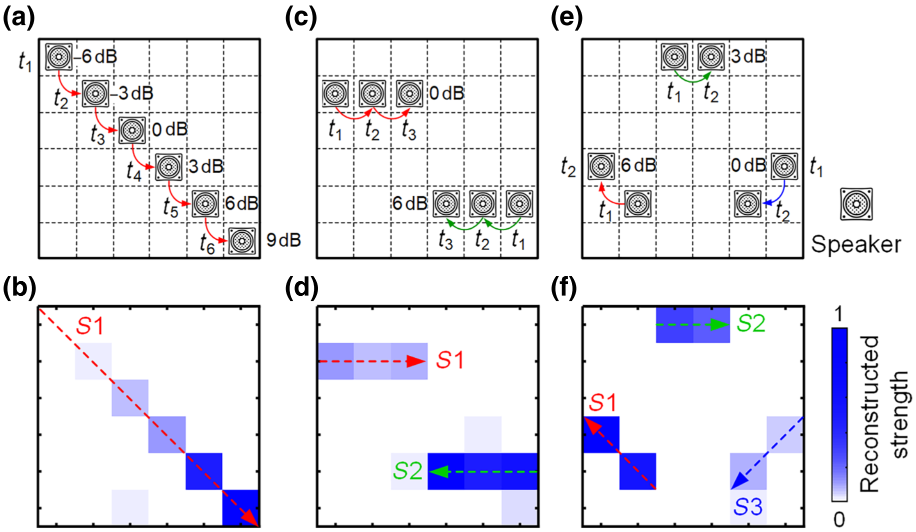

FIG. 6. Planar acoustic images with amplitude and position information. (a) Schematic of the imaging task for a single source with different amplitudes and positions at six moments. (b) Reconstruction result of the moving source. (c), (e) Imaging tasks for two and three different sources with different amplitudes, respectively. (d), (f) Reconstructed acoustic images of multiple sources. The gradation of the color bar is logarithmic to improve the visualization. The paths of the sources in (b), (d), and (f) are denoted as $S1$, $S2$, and $S3$, respectively, and marked by dotted arrows.

from six speakers of the same type at intervals of one second to simulate a moving source. The relative amplitudes of the signal at the six moments (t_1–t_6) are $-6 \sim 9$ dB, respectively. Figure 6(b) shows the superposition of the reconstruction results at each moment. The path (denoted as $S1$ and marked by the dotted arrow) and strength of the moving sound source can be clearly reflected from the acoustic image. Details of the reconstructed image at each moment can be found in Fig. S7 of the Supplemental Material [39]. In the second task, two different testing signals are simultaneously emitted at three moments (t_1–t_3) as shown in Fig. 6(c). The relative amplitudes of the testing signals are 0 and 6 dB, respectively. The reconstructed acoustic image in Fig. 6(d) shows two sound sources moving in opposite directions with different amplitudes (denoted as $S1$ and $S2$). The third task illustrated in Fig. 6(e) is similar to the second task but using three different testing signals, and the results are shown in Fig. 6(f). The above reconstruction tasks demonstrate that the designed metamaterial-based single-detector acoustic camera can yield an acoustic image with amplitude and position information, which has application prospects in tracking drones or other targets.

III. DISCUSSION

The anisotropic acoustic property of the designed space-coiling metamaterial produces the orthogonal directional modulation of the incident sound waves, which is the physical basis for realizing a single-detector acoustic compressive imaging. Experimental results demonstrate that the metamaterial-based single-detector acoustic camera can realize azimuthal and planar acoustic compressive imaging with high recognition ratios. Incorrect recognitions may be due to one signal being overwhelmed by the other signals and unavoidable background noises. Nonetheless, the proposed design can still be satisfactory for acoustic imaging tasks. The device should be protected from ambient noises when performing in a real-world situation. Reticulated or fluffy windshields can be placed around the device to reduce noise interference during the measurement. In addition, algorithms that can reduce background noises can be included in the signal processing procedure.

The proposed metamaterial-based single-detector acoustic camera has several features that distinguish it from other acoustic imaging approaches. Compared to a conventional acoustic camera based on microphone arrays, the proposed design reduces the system complexity and dimensions while ensuring the accuracy of the acoustic imaging. The resolution of a regular microphone array can be estimated by $\Delta x = z\lambda/(D_A \cos^3\theta)$, where z is the distance between the array and the objective plane, D_A is the aperture size of the array, and θ is the off-axis angle [42]. The bandwidth is approximately 730 Hz for a cross array with 40 microphones and a D_A of 1 m to obtain the same resolution as that of the proposed device ($\Delta x = 0.14$ m) (see Supplemental Material [39]). In contrast, the proposed single-detector acoustic camera is approximately $0.19 \times 0.15 \times 0.11$ m^3 with a bandwidth greater than 2000 Hz, and it is fabricated by 3D printing. The proposed design outperforms the microphone array in terms of dimension, bandwidth, and cost. The design can be easily shared and modified on the basis of actual needs because it can be implemented by 3D printing.

Moreover, the passive multiple broadband source localization and separation of the metamaterial-based single-detector acoustic camera is the main advantage over the bionic microphones and other directional acoustic sensors relying on active scanning. Different from the metamaterial multispeaker listener with Helmholtz resonator arrays in Ref. [35], the directional modulation of the sound waves is realized by the space-coiling method. The height of the metamaterial can be designed so small that planar imaging can be realized by stacking different metamaterial samples without making the overall size too large. In addition, the miniaturization of the proposed device is practical with the help of advanced manufacturing methods (e.g., microfabrication or stereo lithography appearance). The folding rate and the number of the acoustic channels can be further increased to improve the spatial resolution of the acoustic imaging. In addition to the current assembly form of the metamaterial modules, the device can also be fabricated as a spherical structure for omnidirectional acoustic imaging. Based on the improvements in both dimensions and spatial resolution, the objective space can be finely meshed to realize a more accurate acoustic imaging.

Furthermore, expanding the audio library is important to extend the applications of the metamaterial device. Various types of broadband acoustic signals (e.g., engine sounds and impulsive noises) in addition to the bird tweets can be included in the audio library as needed. The device can be used in specific cases such as structural impact detection and target tracking, where the signal structures are similar in general. When the device receives enough data, feature extraction and pattern recognition can be performed by introducing data-driven algorithms. With the further study of advanced algorithms, the recognition and localization of unfamiliar sound sources can also be realized.

IV. CONCLUSION

We demonstrate a space-coiling anisotropic metamaterial for realizing a single-detector acoustic camera, which can achieve a multiple broadband source imaging. We envision that the metamaterial-based single-detector acoustic camera can be integrated with numerous systems, such as handheld devices and robotic systems. The application of the metamaterial-based single-detector acoustic camera brings alternative opportunities in the fields of acoustic engineering, including acoustic target tracking, structural health monitoring, and medical imaging.

ACKNOWLEDGMENTS

This work was supported by the National Natural Science Foundation of China (Grants No. 11872244 and No. 51475441), the Youth Innovation Promotion Association CAS (Grant No. 2016396), and the Fundamental Research Funds for the Central Universities in China. T. J. thanks Kesai Ouyang and Wei Xiong for useful discussions.

APPENDIX A: TRANSMISSIONS OF THE EFFECTIVE MODEL

1. Analytical derivations

The TMM is performed to investigate the transmission of the acoustic channel module in the space-coiling metamaterial. Here, the viscous and thermal effects are not taken into consideration for convenience of the derivation. Figure 7(a) shows an effective model of the nth unit cell in an acoustic channel module. The effective refractive index and effective mass density of the nth unit cell are given by Eqs. (1) and (2). The acoustic pressure and velocity at boundary R_n are defined as p_n and $\mathbf{v}_n$, respectively. The acoustic equation of the fan-shaped area can be described by Webster's horn equation, which is expressed in the form of velocity potential:

$$\left(\frac{\partial^2}{\partial r^2} + m\frac{\partial}{\partial r} + k^2\right)\Phi = 0, \tag{A1}$$

where r is the coordinate along the axial direction; m is the flare constant; Φ is the velocity potential; the wave number is $k = \omega/c$, where ω is the angular frequency and c is

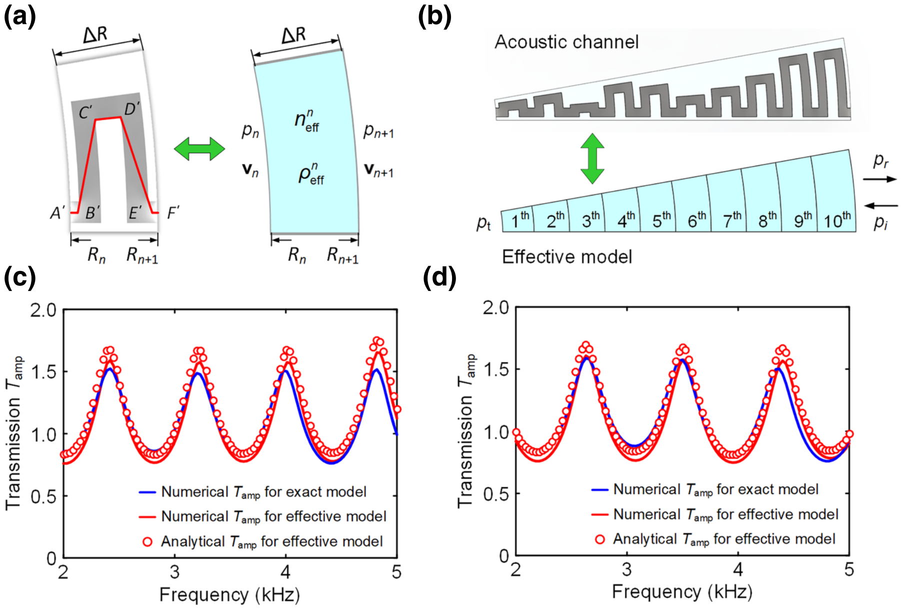

FIG. 7. Effective model and transmission of the acoustic channel module. (a) The effective model of the nth unit cell. The acoustic wave trajectory is marked by red solid lines $A'B'C'D'E'F'$. (b) The effective model of the acoustic channel module. (c), (d) Comparison between the analytic results from the transfer matrix method and the numerical results of two different acoustic channel modules.

the speed of sound. The boundary length of the unit cell is $S = r\alpha$. The flare constant m can be expressed as

$$m = \frac{\partial \ln S}{\partial r} = \frac{1}{S}\frac{\partial S}{\partial r} = \frac{1}{r}\,. \tag{A2}$$

The solution of Eq. (A1) has the form

$$\Phi = C_1 e^{\mu_1 r} + C_2 e^{\mu_2 r}, \tag{A3}$$

$$\mu_1 = \frac{-m + i\sqrt{4k^2 - m^2}}{2}, \tag{A4}$$

$$\mu_2 = \frac{-m - i\sqrt{4k^2 - m^2}}{2}\,. \tag{A5}$$

From the velocity potential in Eq. (A3), the acoustic pressure and the velocity can be calculated as

$$p = -\rho\frac{\partial \Phi}{\partial t} = -i\rho\omega(C_1 e^{\mu_1 r} + C_2 e^{\mu_2 r})\,, \tag{A6}$$

$$\mathbf{v} = \frac{\partial \Phi}{\partial r} = C_1\mu_1 e^{\mu_1 r} + C_2\mu_2 e^{\mu_2 r}\,, \tag{A7}$$

where C_1 and C_2 are coefficients to be determined. For the effective unit cell, the speed of sound c should be expressed as $c^n_{\text{eff}} = c_0/n^n_{\text{eff}}$, where c_0 is the sound speed in air. The acoustic pressure and velocity at boundaries R_n and R_{n+1} can be given by

$$\begin{cases} p_n = -i\rho^n_{\text{eff}}\omega(C^n_1 e^{\mu^n_1 R_n} + C^n_2 e^{\mu^n_2 R_n}), \\ \mathbf{v}_n = C^n_1\mu^n_1 e^{\mu^n_1 R_n} + C^n_2\mu^n_2 e^{\mu^n_2 R_n}, \end{cases} \tag{A8}$$

$$\begin{cases} p_{n+1} = -i\rho^n_{\text{eff}}\omega(C^n_1 e^{\mu^n_1 R_{n+1}} + C^n_2 e^{\mu^n_2 R_{n+1}}), \\ \mathbf{v}_{n+1} = C^n_1\mu^n_1 e^{\mu^n_1 R_{n+1}} + C^n_2\mu^n_2 e^{\mu^n_2 R_{n+1}}. \end{cases} \tag{A9}$$

Here, the n in the subscripts and superscripts denotes the parameters belonging to the nth unit cell. The coefficients C^n_1 and C^n_2 can be derived from Eq. (A8) and represented by p_n and $\mathbf{v}_n$ as follows:

$$\begin{cases} C^n_1 = \dfrac{\mu^n_2 p_n + i\rho^n_{\text{eff}}\omega\mathbf{v}_n}{-i\rho^n_{\text{eff}}\omega(\mu^n_2 - \mu^n_1)e^{\mu^n_1 R_n}}, \\ C^n_2 = \dfrac{\mu^n_1 p_n + i\rho^n_{\text{eff}}\omega\mathbf{v}_n}{-i\rho^n_{\text{eff}}\omega(\mu^n_1 - \mu^n_2)e^{\mu^n_2 R_n}}. \end{cases} \tag{A10}$$

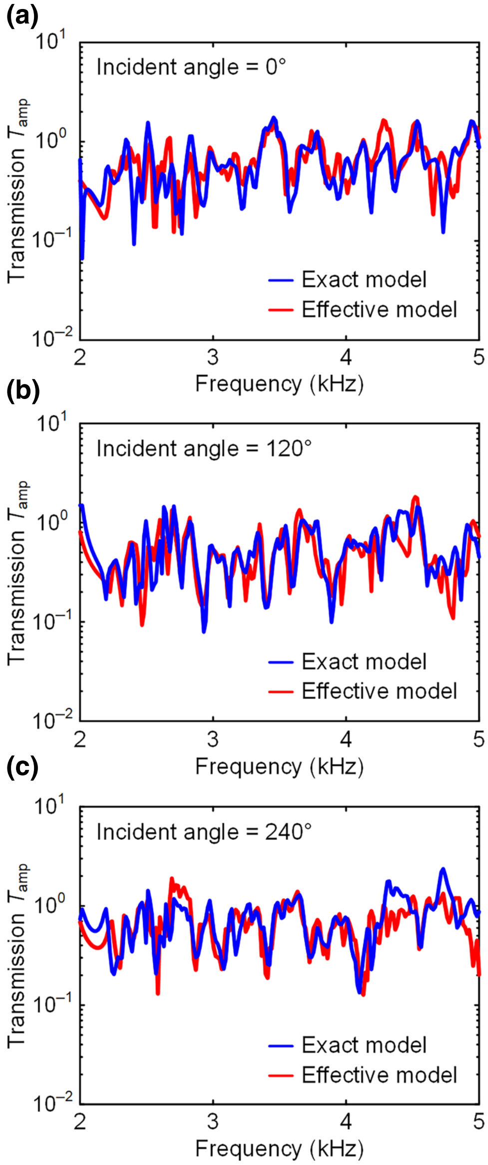

FIG. 8. Comparison between the exact model and the effective model of the entire space-coiling metamaterial. The transmissions of the exact model and the effective model when incident angles are (a) 0°, (b) 120°, and (c) 240°, respectively.

By substituting Eq. (A10) into Eq. (A9), the relationship between the acoustic pressures and the velocities at boundaries R_n and R_{n+1} can be expressed as

$$\begin{Bmatrix} p_{n+1} \\ \mathbf{v}_{n+1} \end{Bmatrix} = [T_n]\begin{Bmatrix} p_n \\ \mathbf{v}_n \end{Bmatrix}\,. \tag{A11}$$

Here, the transfer matrix $[T_n]$ of the nth unit cell is given by

$$[T_n] = \begin{bmatrix} \frac{1}{\mu^n_2 - \mu^n_1}\left(\mu^n_2 e^{\mu^n_1\Delta R} - \mu^n_1 e^{\mu^n_2\Delta R}\right) & \frac{i\rho^n_{\text{eff}}\omega}{\mu^n_2 - \mu^n_1}\left(e^{\mu^n_1\Delta R} - e^{\mu^n_2\Delta R}\right) \\ \frac{i\mu^n_1\mu^n_2}{\rho^n_{\text{eff}}\omega(\mu^n_2 - \mu^n_1)}\left(e^{\mu^n_1\Delta R} - e^{\mu^n_2\Delta R}\right) & \frac{-1}{\mu^n_2 - \mu^n_1}\left(\mu^n_1 e^{\mu^n_1\Delta R} - \mu^n_2 e^{\mu^n_2\Delta R}\right) \end{bmatrix}. \tag{A12}$$

Figure 7(b) shows an effective model of an acoustic channel module. The module is comprised of 10 effective unit cells with different effective acoustic parameters. Thus, the transfer relationship of the module can be given by

$$\begin{Bmatrix} p_{11} \\ \mathbf{v}_{11} \end{Bmatrix} = [T_{10}]\cdots[T_1]\begin{Bmatrix} p_1 \\ \mathbf{v}_1 \end{Bmatrix} = \begin{bmatrix} M_{11} & M_{12} \\ M_{21} & M_{22} \end{bmatrix}\begin{Bmatrix} p_1 \\ \mathbf{v}_1 \end{Bmatrix}, \tag{A13}$$

where M_{11}, M_{12}, M_{21}, and M_{22} are elements of the overall transfer matrix of the module. By employing the boundary conditions, the transmission coefficient of the module can be obtained. At boundary R_{11},

$$\begin{cases} p_{11} = p_i + p_r, \\ \mathbf{v}_{11} = \frac{1}{\rho_0 c_0}(p_i - p_r). \end{cases} \tag{A14}$$

At boundary R_1,

$$\begin{cases} p_1 = p_t, \\ \mathbf{v}_1 = \frac{1}{\rho_0 c_0} p_t. \end{cases} \tag{A15}$$

From Eqs. (A13) to (A15), the complex transmission coefficient T is derived as

$$T = \frac{p_t}{p_i} = \frac{2}{M_{11} + M_{12}/\rho_0 c_0 + \rho_0 c_0 M_{21} + M_{22}}. \tag{A16}$$

The amplitude of the transmission coefficient can be obtained as $T_{\text{amp}} = |T|$.

2. Comparison between the effective model and the exact model

Two different modules are investigated by using the TMM. Parameters of these two modules are shown in Table S1 [39]. Full-wave numerical simulations are also performed to calculate the transmissions of the exact model and the effective model by using the acoustic module in COMSOL Multiphysics. All simulations are done in two dimensions, where the viscous and thermal losses are not taken into consideration. The results are shown in Figs. 7(c) and 7(d). It can be observed that the analytical results from the TMM are in agreement with the numerical results of the exact model and the effective model. The transmissions of different modules are orthogonal due to the stochastic effective parameters of the unit cells. This randomness of the effective parameter is ultimately attributed to the randomness of angle β_n in the unit cell, which makes the metamaterial highly anisotropic.

The directional frequency spectra of the entire metamaterial-based single-detector acoustic camera and the effective model in Fig. 1(c) are also obtained from numerical simulations. The effective acoustic parameters of the effective model are provided in Table S2 [39]. Figure 8 shows the transmissions of the entire exact model and the effective model when the incident angles are 0°, 120°, and 240°, respectively. The transmissions of the effective model are consistent with the exact model, indicating that the effective model can accurately reflect the anisotropic acoustic property of the space-coiling metamaterial.

APPENDIX B: CONSTRUCTION OF THE MEASUREMENT MATRIX

The measurement matrix **M** includes information of the directional frequency response of the metamaterial and the contents of the testing signals in the audio library. The directional frequency response of the metamaterial is

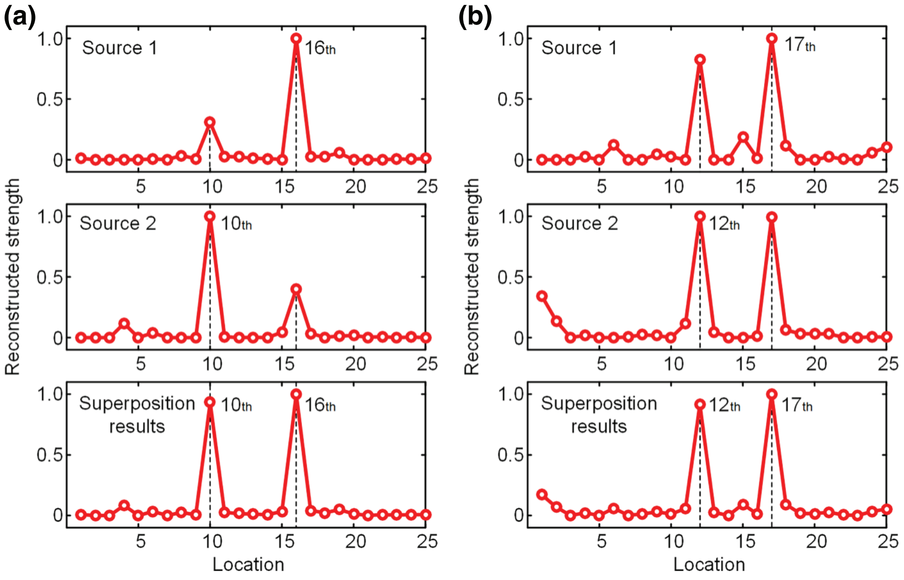

FIG. 9. Details of the reconstruction results for planar acoustic imaging. (a) Reconstruction results for Source 1 and Source 2 when they are located at the 16th and 10th grids. (b) Reconstruction results for the two sources when they are located at the 17th and 12th grids.

defined as $\mathbf{h}_p(\omega)$, where p is the number of the source location and ω is the angular frequency. The testing signal in the audio library is defined as $\mathbf{r}_q(\omega)$, where q presents the signal label in the audio library. The matrices **M**, **H**, and **R** can be represented in the form of column vectors, namely $\mathbf{M} = [\mathbf{m}_j]$, $\mathbf{H} = [\mathbf{h}_p]$, and $\mathbf{R} = [\mathbf{r}_q]$, respectively. The measurement matrix is constructed as $[\mathbf{m}_j] = [\mathbf{h}_p \cdot \mathbf{r}_q]$, where the subscripts j, p, and q are free indices in the index notation. Thus, the number of the columns of the matrix **M** is $j = p \times q$.

APPENDIX C: RECONSTRUCTED STRENGTH ANALYSIS OF PLANAR ACOUSTIC IMAGING

The objective plane is meshed and numbered as shown in Fig. 5(c). Two cases of the planar multiple source imaging results are demonstrated in Fig. 9. When two sources are far apart (e.g., the sources are in the 10th and 16th grids), we can distinguish which source is located at what position by comparing the substantial difference in the reconstructed strength. It can be seen that the reconstructed strength of the 16th element is stronger than that of the 10th element for Source 1 as shown in Fig. 9(a). Conversely, the reconstructed strength of the 16th element is weaker than that of the 10th element for Source 2. Therefore, we can determine that Source 1 is located at the 16th grid and Source 2 is located at the 10th grid. The imaging result in Fig. 5(e) of the main text is the superposition of the reconstruction results for Source 1 and Source 2. When two sources are too close to each other (e.g., the sources are in the 17th and 12th grids), the difference of the reconstructed strength is so small that the sources cannot be distinguished as shown in Fig. 9(b).

[1] M. Erol-Kantarci, H. T. Mouftah, and S. Oktug, A survey of architectures and localization techniques for underwater acoustic sensor networks, IEEE Commun. Surv. Tut. **13**, 487 (2011).

[2] J. Shin and L. Huang, Spatial prediction filtering of acoustic clutter and random noise in medical ultrasound imaging, IEEE Trans. Med. Imaging **36**, 396 (2017).

[3] E. Cardenas Cabada, Q. Leclere, J. Antoni, and N. Hamzaoui, Fault detection in rotating machines with beamforming: spatial visualization of diagnosis features, Mech. Syst. Signal Processing **97**, 33 (2017).

[4] J. Billingsley and R. Kinns, The acoustic telescope, J. Sound Vib. **48**, 485 (1976).

[5] T. F. Brooks, M. A. Marcolini, and D. S. Pope, A directional array approach for the measurement of rotor noise source distributions with controlled spatial resolution, J. Sound Vib. **112**, 192 (1987).

[6] T. F. Brooks and W. M. Humphreys, A deconvolution approach for the mapping of acoustic sources (DAMAS) determined from phased microphone arrays, J. Sound Vib. **294**, 856 (2006).

[7] M. Legg and S. Bradley, A combined microphone and camera calibration technique with application to acoustic imaging, IEEE Trans. Image Processing **22**, 4028 (2013).

[8] R. N. Miles, D. Robert, and R. R. Hoy, mechanically coupled ears for directional hearing in the parasitoid fly Ormia ochracea, J. Acoust. Soc. Am. **98**, 3059 (1995).

[9] H. Liu, L. Currano, D. Gee, T. Helms, and M. Yu, Understanding and mimicking the dual optimality of the fly ear, Sci. Rep. **3**, 2489 (2013).

[10] A. P. Vedurmudi, J. Goulet, J. Christensen-Dalsgaard, B. A. Young, R. Williams, and J. L. v. Hemmen, How Internally Coupled Ears Generate Temporal and Amplitude Cues for Sound Localization, Phys. Rev. Lett. **116**, 028101 (2016).

[11] Y. Chen, H. Liu, M. Reilly, H. Bae, and M. Yu, Enhanced acoustic sensing through wave compression and pressure amplification in anisotropic metamaterials, Nat. Commun. **5**, 5247 (2014).

[12] X. Zhu, B. Liang, W. Kan, Y. Peng, and J. Cheng, Deep-Subwavelength-Scale Directional Sensing Based on Highly Localized Dipolar Mie Resonances, Phys. Rev. Appl. **5**, 054015 (2016).

[13] T. Jiang, Q. He, and Z.-K. Peng, Enhanced directional acoustic sensing with phononic crystal cavity resonance, Appl. Phys. Lett. **112**, 261902 (2018).

[14] J. Hunt, T. Driscoll, A. Mrozack, G. Lipworth, M. Reynolds, D. Brady, and D. R. Smith, Metamaterial apertures for computational imaging, Science **339**, 310 (2013).

[15] C. M. Watts, D. Shrekenhamer, J. Montoya, G. Lipworth, J. Hunt, T. Sleasman, S. Krishna, D. R. Smith, and W. J. Padilla, Terahertz compressive imaging with metamaterial spatial light modulators, Nat. Photonics **8**, 605 (2014).

[16] D. B. Phillips, M.-J. Sun, J. M. Taylor, M. P. Edgar, S. M. Barnett, G. M. Gibson, and M. J. Padgett, Adaptive foveated single-pixel imaging with dynamic supersampling, Sci. Adv. **3**, e1601782 (2017).

[17] J. S. Rogers, C. A. Rohde, M. D. Guild, C. J. Naify, T. P. Martin, and G. J. Orris, Demonstration of acoustic source localization in air using single pixel compressive imaging, J. Appl. Phys. **122**, 214901 (2017).

[18] J. Yin, C. Tao, and X. Liu, Dynamic focusing of acoustic wave utilizing a randomly scattering lens and a single fixed transducer, J. Appl. Phys. **121**, 174901 (2017).

[19] P. Kruizinga, P. van der Meulen, A. Fedjajevs, F. Mastik, G. Springeling, N. de Jong, J. G. Bosch, and G. Leus, Compressive 3d ultrasound imaging using a single sensor, Sci. Adv. **3**, e1701423 (2017).

[20] G. Ma and P. Sheng, Acoustic metamaterials: From local resonances to broad horizons, Sci. Adv. **2**, e1501595 (2016).

[21] S. A. Cummer, J. Christensen, and A. Alù, Controlling sound with acoustic metamaterials, Nat. Rev. Mater. **1**, 16001 (2016).

[22] H. Ge, M. Yang, C. Ma, M.-H. Lu, Y.-F. Chen, N. Fang, and P. Sheng, Breaking the barriers: Advances in acoustic functional materials, Natl. Sci. Rev. **5**, 159 (2017).

[23] Z. Liu, X. Zhang, Y. Mao, Y. Y. Zhu, Z. Yang, C. T. Chan, and P. Sheng, Locally resonant sonic materials, Science **289**, 1734 (2000).

[24] N. Fang, D. Xi, J. Xu, M. Ambati, W. Srituravanich, C. Sun, and X. Zhang, Ultrasonic metamaterials with negative modulus, Nat. Mater. **5**, 452 (2006).

[25] Z. Liang and J. Li, Extreme Acoustic Metamaterial by Coiling up Space, Phys. Rev. Lett. **108**, 114301 (2012).

[26] R. Zhu, X. N. Liu, G. K. Hu, C. T. Sun, and G. L. Huang, Negative refraction of elastic waves at the deep-subwavelength scale in a single-phase metamaterial, Nat. Commun. **5**, 5510 (2014).

[27] S. Zhang, C. Xia, and N. Fang, Broadband Acoustic Cloak for Ultrasound Waves, Phys. Rev. Lett. **106**, 024301 (2011).

[28] C. Shen, J. Xu, N. X. Fang, and Y. Jing, Anisotropic Complementary Acoustic Metamaterial for Canceling out Aberrating Layers, Phys. Rev. X **4**, 041033 (2014).

[29] L. Zigoneanu, B. I. Popa, and S. A. Cummer, Three-dimensional broadband omnidirectional acoustic ground cloak, Nat. Mater. **13**, 352 (2014).

[30] B. Xie, K. Tang, H. Cheng, Z. Liu, S. Chen, and J. Tian, Coding acoustic metasurfaces, Adv. Mater. **29**, 1603507 (2017).

[31] Y. Zhu, X. Fan, B. Liang, J. Cheng, and Y. Jing, Ultrathin Acoustic Metasurface-Based Schroeder Diffuser, Phys. Rev. X **7**, 021034 (2017).

[32] P. Wang, F. Casadei, S. Shan, J. C. Weaver, and K. Bertoldi, Harnessing Buckling to Design Tunable Locally Resonant Acoustic Metamaterials, Phys. Rev. Lett. **113**, 014301 (2014).

[33] S. Babaee, N. Viard, P. Wang, N. X. Fang, and K. Bertoldi, Harnessing deformation to switch on and off the propagation of sound, Adv. Mater. **28**, 1631 (2016).

[34] O. R. Bilal, A. Foehr, and C. Daraio, Bistable metamaterial for switching and cascading elastic vibrations, Proc. Natl. Acad. Sci. **114**, 4603 (2017).

[35] Y. Xie, T.-H. Tsai, A. Konneker, B.-I. Popa, D. J. Brady, and S. A. Cummer, Single-sensor multispeaker listening with acoustic metamaterials, Proc. Natl. Acad. Sci. U.S.A. **112**, 10595 (2015).

[36] R. Al Jahdali and Y. Wu, High transmission acoustic focusing by impedance-matched acoustic meta-surfaces, Appl. Phys. Lett. **108**, 031902 (2016).

[37] R. Ghaffarivardavagh, J. Nikolajczyk, R. G. Holt, S. Anderson, and X. Zhang, Horn-like space-coiling metamaterials toward simultaneous phase and amplitude modulation, Nat. Commun. **9**, 1349 (2018).

[38] J. Zhao, R. Al Jadhali, L. Zhang, and Y. Wu, Directional sound beam emission from a configurable compact multi-source system, Sci. Rep. **8**, 1018 (2018).

[39] See Supplemental Material at http://link.aps.org/supplemental/10.1103/PhysRevApplied.11.034013 for additional figures and notes, and parameters of acoustic channel modules.

[40] M. Molerón, M. Serra-Garcia, and C. Daraio, Visco-thermal effects in acoustic metamaterials: From total transmission to total reflection and high absorption, New J. Phys. **18**, 033003 (2016).

[41] J. M. Bioucas-Dias and M. A. Figueiredo, A new TWIST: Two-step iterative shrinkage/thresholding algorithms for image restoration, IEEE Trans. Image Processing **16**, 2992 (2007).

[42] J. Christensen and J. Hald, *Beamforming* (Bruel & Kjaer, Denmark, 2004), Technical Review.